lubricants

MDPI

Article

Frictional Behavior and Fluid Flow Simulation Analysis of Textured ZrO_2–Polyetheretherketone Artificial Knee Joints

Liwei Jiang [1], Bo Li [2], Fanshuo Jia [1], Guangjie Wang [1], Yayun Liu [1,*], Kedong Zhang [1], Ning Jiang [1] and Chuanyang Wang [1,*]

[1] School of Mechanical and Electric Engineering, Soochow University, Suzhou 215021, China; lwjiang0705@stu.suda.edu.cn (L.J.)
[2] Department of Mechanical and Electrical Engineering, Yangquan Vocational and Technical College, Yangquan 045000, China; 18935322211@189.cn
* Correspondence: yyliu6688@suda.edu.cn (Y.L.); cywang@suda.edu.cn (C.W.); Tel.: +86-15562637056 (Y.L.)

Abstract: ZrO_2 ceramics, known for their high strength and wear resistance, are ideal for artificial joints. This study enhanced the friction performance of these joints by fabricating textured structures (50 μm width and 20–25 μm depth) on the ceramic surface. Friction tests, conducted at 200 r/min for 30 min with a 5–20 N load and lubricant concentration of 15–60 mg/mL using PEEK balls, showed that textured joints outperformed untextured ones. The symmetrical triangular structure had the lowest coefficient of friction and the best hydrophilicity, with a 53.0% reduction in the coefficient of friction and a 57.4% reduction in the contact angle compared to the untextured structure. The textures effectively store the PEEK residue and facilitate the smooth movement of the worn ball. Concurrently, the textured structure stores some of the lubricant, which reduces the static pressure during fluid flow by 12.6%. Overall, the friction performance of ZrO_2 ceramic artificial joints was significantly improved by the textured structures.

Keywords: texture; fluid flow simulation; lubricants; friction; wear; surface wettability

check for updates

Received: 2 December 2024
Revised: 27 December 2024
Accepted: 7 January 2025
Published: 8 January 2025

Citation: Jiang, L.; Li, B.; Jia, F.; Wang, G.; Liu, Y.; Zhang, K.; Jiang, N.; Wang, C. Frictional Behavior and Fluid Flow Simulation Analysis of Textured ZrO_2–Polyetheretherketone Artificial Knee Joints. *Lubricants* **2025**, *13*, 23. https://doi.org/10.3390/lubricants13010023

Copyright: © 2025 by the authors. Licensee MDPI, Basel, Switzerland. This article is an open access article distributed under the terms and conditions of the Creative Commons Attribution (CC BY) license (https://creativecommons.org/licenses/by/4.0/).

1. Introduction

The demand for artificial knee joints is increasing dramatically due to the high demands placed on the knee joints in sports and the fact that sports injuries and various diseases can affect the normal use of the knee joints [1,2]. The service life of an artificial knee joint is closely related to its frictional wear characteristics. Among the various forms of wear and tear of the artificial knee joint, the frictional wear characteristics between the joint surfaces play a crucial role in prolonging its service life [3–5]. At the same time, wear resistance and biocompatibility are important for implant stability [6]. Therefore, improving the wear resistance of artificial knee materials while considering their biocompatibility is a key issue to improve longevity and stability [7].

Polyetheretherketone (PEEK) is a high-performance polymer that exhibits excellent mechanical properties and biocompatibility. It is a favoured material for use in medical implants due to its good resistance to high temperatures and chemicals, as well as its excellent mechanical strength [8–10]. Similarly, zirconia (ZrO_2) ceramics exhibit notable advantages over traditional metal alloys as implant materials in the biomedical field [11]. Their exceptional biocompatibility minimises the risk of immune rejection and facilitates the long-term integration of the implant into the surrounding tissue [12]. ZrO_2 ceramics exhibit favourable abrasion resistance and a low coefficient of friction, which serves to

minimise wear on the prosthetic surface and thereby extend the service life of the prosthesis [13]. Furthermore, its high tensile strength and resistance to corrosion guarantee stability within the internal environment. Additionally, its aesthetic properties are comparable to those of natural bone, which has led to a diverse range of applications in fields such as dentistry [14,15]. In conclusion, ZrO_2 ceramics have the potential to enhance the functionality and durability of medical implants.

Recent studies have demonstrated that surface texture structures exert a considerable beneficial influence on the friction and wear performance of medical implants, particularly in applications such as artificial joints and dental implants [16,17]. The optimisation of the texture structure of the implant surface has the potential to significantly reduce friction and wear, thereby extending the service life of the implant. Furthermore, it has the capacity to improve the distribution of lubricants and reduce contact pressure, which, in turn, can enhance the overall performance of the implant [18,19]. The design of this surface texture serves two purposes; firstly, it improves the biocompatibility of the implant and secondly, it facilitates the integration of the implant site with the surrounding tissue [20–22]. Furthermore, surface texture structures are commonly employed in cutting tools to enhance both tool longevity and machining efficiency. Previous studies have used textures such as triangular, striped, and rhombic structures for surface modification, which are used to improve tool life and machining efficiency by reducing the friction generated during the cutting process [23–26]. Consequently, surface texture optimisation techniques have been shown to have considerable application value in a number of fields, particularly in the context of medical implants and cutting tools. The current research on different texture structures is relatively complete. Optimising the surface design of artificial knee joints can address the problem of early implant failure due to friction and wear in the clinic. Incorporating surface textures can not only improve the smoothness of joint movement, but also effectively extend the life of the artificial knee joint, reducing the risk and cost of secondary surgery for patients. Especially in sports medicine and geriatrics, the need for durability and stability is urgent, so optimising the surface structure of the artificial knee joint is of great clinical importance and practical value. Currently, there is a lack of systematic studies investigating how textured structures influence the fluid flow state of lubricants during friction and wear, which limits the comprehensive understanding of the wear reduction mechanism. This work aims to investigate the fluid flow state to reveal how textured structures contribute to wear reduction, providing some theoretical basis for the design of high-performance artificial knee joints.

In this study, ZrO_2 ceramics and PEEK were selected as the materials for artificial knee joints. Three different surface texture structures (rhombic, symmetric triangular, and stripped structures) were prepared using nanosecond laser technology with the aim of improving the friction and wear performance of the implants. The impact of varying surface textures, load levels, and lubricant concentrations on the friction and wear characteristics of artificial knee joints was examined. Furthermore, the influence of surface texture structures on the hydrodynamic properties of the lubricant during friction was investigated, and the potential mechanisms through which they may enhance the friction and wear performance of ZrO_2–PEEK artificial knee joints were analysed.

2. Materials and Methods

2.1. Materials

In the course of the experiments, a tetragonal ZrO_2 ceramic plate and PEEK balls were employed. The dimensions of the ZrO_2 ceramic plate are 25 mm × 25 mm × 3 mm. PEEK balls with a diameter of 6 mm were used to match the size of the friction tester fixture. The

lubricant was composed of bovine serum albumin (BSA) and 1× phosphate-buffered saline (PBS), with a solubility of greater than 60 mg/mL for BSA in 1× PBS.

The texture was processed using a nanosecond laser marking machine, as shown in Figure 1. The current was 1 A, the processing speed was 100 µm/s, and the pulse frequency was 30 kHz; a spiral scanning strategy was chosen to ensure the quality of the texture. Figure 2 shows the morphology of the three different textures with a depth between 20 and 25 µm. The rhombic texture is designated as "Texture Structure 1" (TS1), the symmetric triangular texture is designated as TS2, and the stripped texture is designated as TS3. The number of processing cycles used was 30 for both TS1 and TS2. In comparison to TS1 and TS2, TS3 had a machining count of 40 to ensure that the depth of the three structures remained at a consistent level.

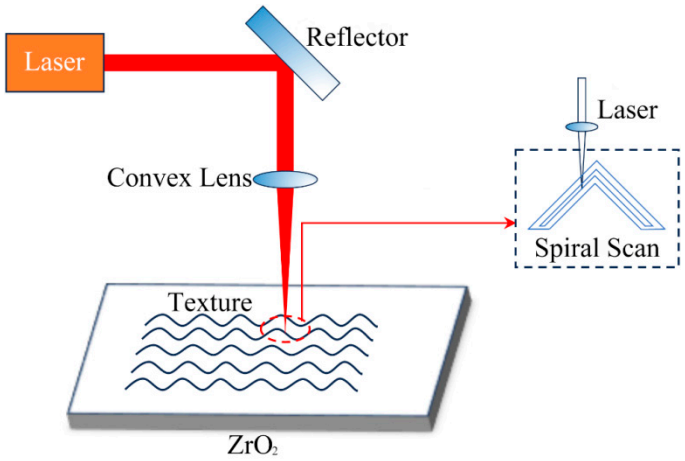

Figure 1. Schematic diagram of nanosecond laser processing.

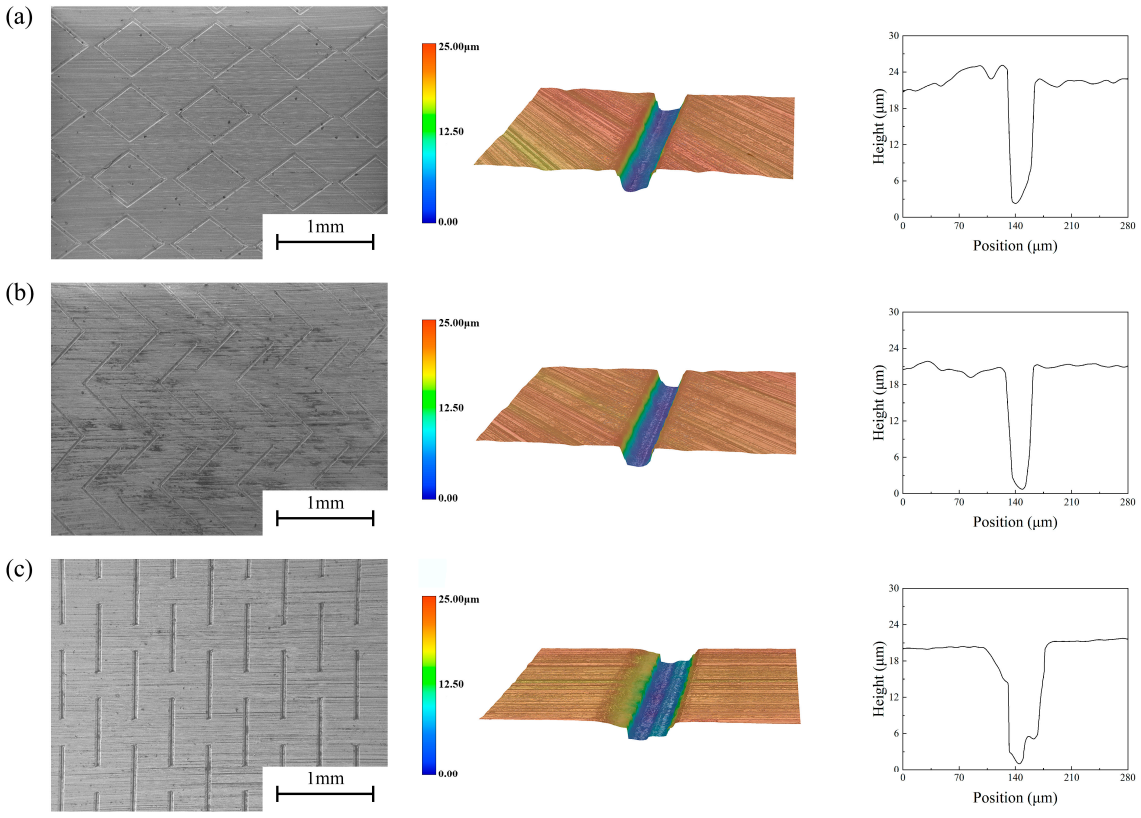

Figure 2. The morphology of the three different micro-textures and their depth. (**a**) TS1, (**b**) TS2, and (**c**) TS3.

2.2. Experimental Methods

In this experiment, the rotary friction tester, with a rotational radius of 2 mm, was used as the experimental equipment. Previous studies have shown that selecting 10 N as the normal load for an artificial joint results in a contact pressure of approximately 100 MPa. The contact pressures generated in the human hip are typically in the range of 10 MPa, whereas the actual contact pressures in hip replacements are much higher than the reported contact pressures [27–29]. Therefore, the load aspect was based on 10 N and 5 N; the selected experimental conditions were 10 N, 15 N, and 20 N. The human body can run about 180 rpm in the running condition, so 200 r/min, which is the closest condition to 180 r/min on the experimental machine, was selected as the experimental condition. A schematic diagram of the experimental equipment is shown in Figure 3. The lubricant was selected to simulate the synovial fluid in the knee joint; it consisted of different BSA concentration solutions (15 mg/mL, 30 mg/mL, 45 mg/mL, and 60 mg/mL). The lubricant was added every 10 min at a dose of 1 mL to ensure that the ball remained in the infiltration state. Wettability is one of the most important properties reflecting the interaction of a solid surface with a liquid. The surface wettability was measured using a contact angle metre (SDC-100). During the test, 10 μL of deionised water was dropped onto the ZrO_2 surface and the drop morphology was captured using a CCD camera. To ensure the accuracy of the image recognition software, the contact angle was calculated semi-automatically with human assistance. In order to ensure the reliability of the results, all experiments in the paper were repeated at least 3 times, and the final results presented are the average of these experimental results.

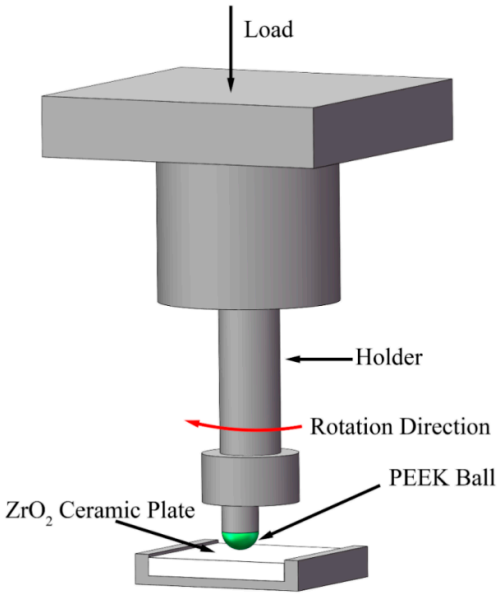

Figure 3. Schematic diagram of rotary friction tester.

In parallel, this study utilises fluid dynamics simulations to investigate the modifications in the flow field induced by the traversal of a PEEK ball over surface textures. Furthermore, scanning electron microscopy (SEM) combined with energy-dispersive X-ray spectroscopy (EDS) was employed to provide a detailed analysis of the underlying mechanisms by which the surface textures contribute to the reduction in frictional wear.

3. Fluid Flow Simulation

3.1. Model Pre-Processing

In this simulation, the overset mesh method is employed to reduce the computational effort and ensure convergence in the motion of the ball. The meshing schematic is illustrated

in Figure 4. Both the foreground and background meshes utilise a hexahedral-structured mesh to ensure the quality of the mesh. The background mesh is only block-divided and refined at the bottom, in proximity to the texture region. In contrast, the foreground mesh is O-divided to ensure the quality of the face mesh on the ball. As no heat transfer is involved, the ball area has been hollowed out in advance to reduce the amount of computation.

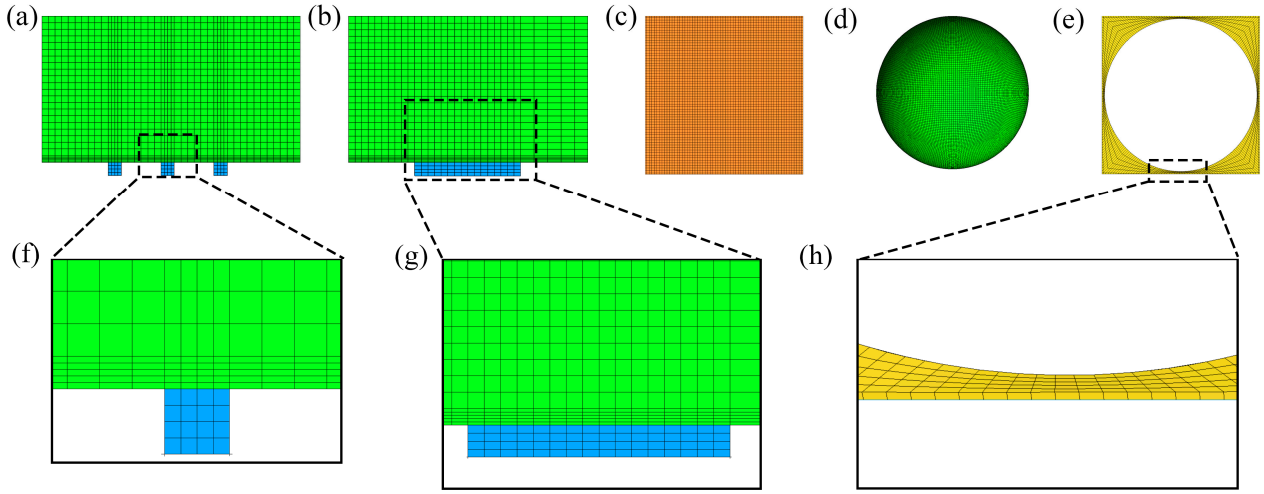

Figure 4. Fluid flow simulation mesh diagram. (**a**) Background mesh for front view. (**b**) Background mesh for side view. (**c**) Outside of the foreground mesh. (**d**) Face mesh of ball inside the foreground mesh. (**e**) Cross-section of the foreground mesh. (**f**) Detail of background mesh for front view. (**g**) Detail of background mesh for side view. (**h**) Detail of the cross-section of the foreground mesh.

3.2. Fluent Setup

In this simulation, after importing the foreground mesh and the background mesh, the overset interface was set up in Fluent. For the coupling of the ball movement region, the speed of motion of the ball is 200 r/min and the radius of motion is 2 mm. In order to simplify the model and simplify the calculation difficulty, as well as to ensure the accuracy of the results, the distance between the bottom surface of the untextured area and the ball is set to 0.5 mm. For lubricants, a 30 mg/mL BSA solution with a density of approximately 1.1 g/cm^3 and a viscosity of approximately 1.22 mPa·s was used for this simulation; the initialised lubricant thickness is 2 mm. The *k*-ε model was chosen for the turbulence modelling aspect due to its insensitivity to initial values, and the turbulent kinetic energy k and the corresponding dissipation ε can be given by two equations [30].

For turbulent kinetic energy k:

$$\frac{\partial(\rho k)}{\partial t} + \frac{\partial(\rho k u_i)}{\partial x_i} = \frac{\partial}{\partial x_j}\left[\frac{\mu_t}{\sigma_k}\frac{\partial k}{\partial x_j}\right] + 2\mu_t E_{ij}E_{ij} - \rho\varepsilon \tag{1}$$

For dissipation ε:

$$\frac{\partial(\rho\varepsilon)}{\partial t} + \frac{\partial(\rho\varepsilon u_i)}{\partial x_i} = \frac{\partial}{\partial x_j}\left[\frac{\mu_t}{\sigma_\varepsilon}\frac{\partial \varepsilon}{\partial x_j}\right] + C_{1\varepsilon}\frac{\varepsilon}{k}2\mu_t E_{ij}E_{ij} - C_{2\varepsilon}\rho\frac{\varepsilon^2}{k} \tag{2}$$

where u_i represents the velocity component in the corresponding direction; E_{ij} represents the component of the rate of deformation; and μ_t represents eddy viscosity, which can be given by:

$$\mu_t = \rho C_\mu \frac{k^2}{\varepsilon} \tag{3}$$

The values of some constants in the equation are given in Table 1.

Table 1. Constants in the *k*-*ε* model.

Constant	Value
C_μ	0.09
σ_k	1.00
σ_ε	1.30
$C_{1\varepsilon}$	1.44
$C_{2\varepsilon}$	1.92

The total number of time steps calculated is 4000, and each time step corresponds to a flow time of 0.005 s.

4. Results and Discussion

4.1. Contact Angles of ZrO_2 Ceramic Plate with Different Micro-Textures

Figure 5 illustrates the magnitude of the contact angle across various textures, with TS0 representing the untreated ZrO_2 ceramic plate. The results indicate that the untreated ZrO_2 ceramic plates exhibit the lowest degree of hydrophilicity. In contrast, the treated ceramic plates demonstrate a significant enhancement in hydrophilicity, with TS2 showing the highest hydrophilicity. This is followed by TS1 and TS3, which exhibit comparable hydrophilic properties, though TS3 shows a marginal increase in hydrophilicity compared to TS1.

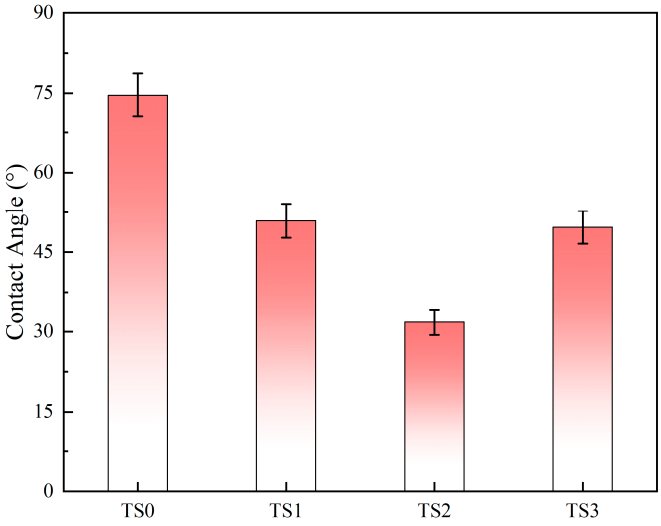

Figure 5. Contact angle for different texture structures.

4.2. Effect of Texture Structure on Friction Properties of ZrO_2–PEEK Artificial Knee Joints

Figure 6a illustrates the friction coefficient curves for different textures at a rotation speed of 200 r/min, a load of 10 N, and a BSA concentration of 30 mg/mL for a period of 30 min. In the absence of surface treatment, the friction coefficient of TS0 exhibited considerable fluctuations, which persisted for the duration of the experiment, including the final 15 min. Furthermore, TS1 exhibits a comparable trend to TS0, albeit with a slightly reduced average friction coefficient. In the case of TS2 and TS3, the fluctuations observed during the initial 15 min were comparable to those observed in TS0 and TS1, with a similar magnitude. However, over the last 15 min, the fluctuations of TS2 and TS3 became more stable, with no significant jumps occurring. In the first 15 min, the bottoms of the balls had not yet been smoothed, resulting in large fluctuations in the friction coefficients for both the textured and untextured structures; however, in the last 15 min, the textured structures stored the residue from the PEEK ball, and the fluctuations in the friction coefficients for

the textured structures were reduced. Figure 6b illustrates the average friction coefficient of different textures over the last 15 min. The average friction coefficient is observed to be larger for TS0 and TS1, which exhibit greater fluctuations in the friction coefficient curve. In contrast, TS2 and TS3, which display smaller fluctuations, exhibit smaller average friction coefficients. The average friction coefficient of TS2 is the lowest among the different textures, and the fluctuation of its friction coefficient in Figure 6a is also relatively minimal.

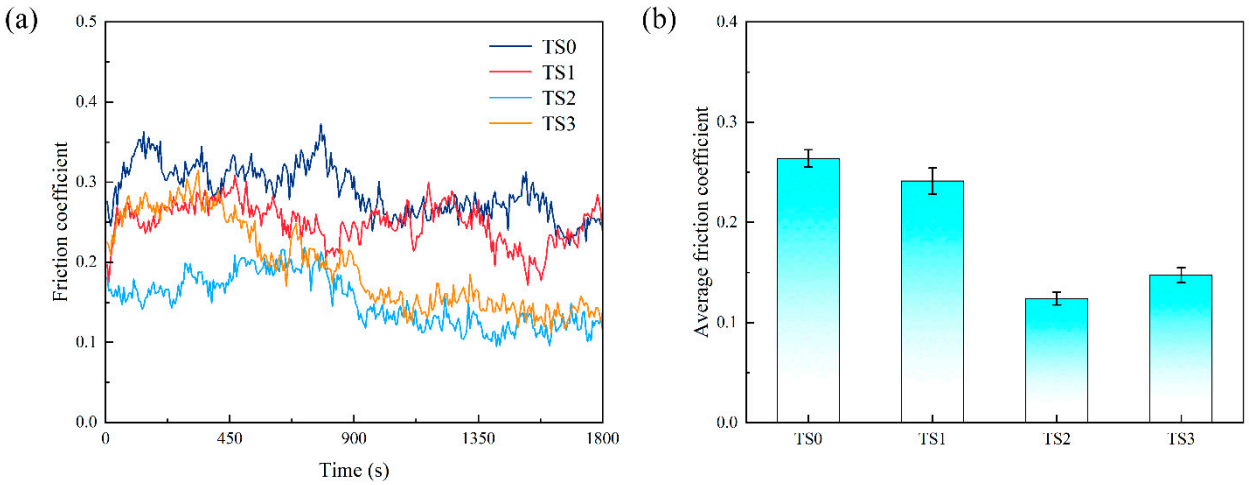

Figure 6. Friction coefficients of different texture structures. (**a**) Curves over 30 min. (**b**) Average friction coefficients in the last 15 min.

When comparing the contact angles under the different textures, there is an approximately linear relationship between the size of the contact angle and the size of the average coefficient of friction in the last 15 min. For TS0, which has the largest contact angle, the hydrophilicity is not as good as the other textures, so the lubricant is more likely to be discharged, resulting in a lower wear-reducing effect of the lubricant and a higher coefficient of friction. The hydrophilicity of TS2 is the best, and the lubricant is more likely to be retained on the friction surface, improving the wear-reducing effect of the lubricant and reducing the coefficient of friction.

4.3. Effect of Load on the Friction Properties of ZrO_2–PEEK Artificial Knee Joints

Figure 7a illustrates the friction coefficients of TS2 under varying loads at a BSA concentration of 30 mg/mL. In the initial 15 min period, the friction coefficient curves exhibited an initial increase, followed by a subsequent decrease when the load sizes were 5 N and 10 N. However, in the last 15 min, the curves demonstrated a tendency towards equilibrium. When the load is 15 N, the overall trend in the friction coefficient curve is not particularly regular, but the overall fluctuation is approximately 0.5, which is smaller than the fluctuation observed during the first 5 min when the load is 5 N. This can be attributed to the fact that at this point in time, the load is already considerable for the PEEK ball, and the ball reaches a relatively stable friction state within a short period of time, which lasts until the conclusion of the experiment. For a load of 20 N, the trend in the initial 15 min is comparable to that observed for loads of 5 N and 10 N. However, in the final 15 min, the friction coefficient exhibits only marginal stability for approximately 10 min, followed by a period of instability in the remaining 5 min. This phenomenon can be attributed to the excessive wear of the smaller balls. Figure 7b illustrates the average friction coefficient over the last 15 min of the experiment. The average friction coefficient demonstrates a tendency to decrease and then increase in response to a gradual increase in load. The average friction coefficient reaches its minimum value at a load of 10 N, after which it exhibits an increasing trend as the load is further increased. This phenomenon can be attributed to the fact that

the torque exerted on the ball exerts a dominant influence on the rise in friction during the ball's movement when the load is relatively minimal. Conversely, as the load is increased, the positive pressure acting on the ball gradually assumes a dominant role in the rise in friction. This phenomenon can be attributed to the fact that when the ball is in motion and subjected to small loads, the torque acting on the ball produces rolling friction, which has the main effect on the overall friction. However, as the load increases, the role of sliding friction gradually becomes more prominent, resulting in the friction decreasing and then increasing.

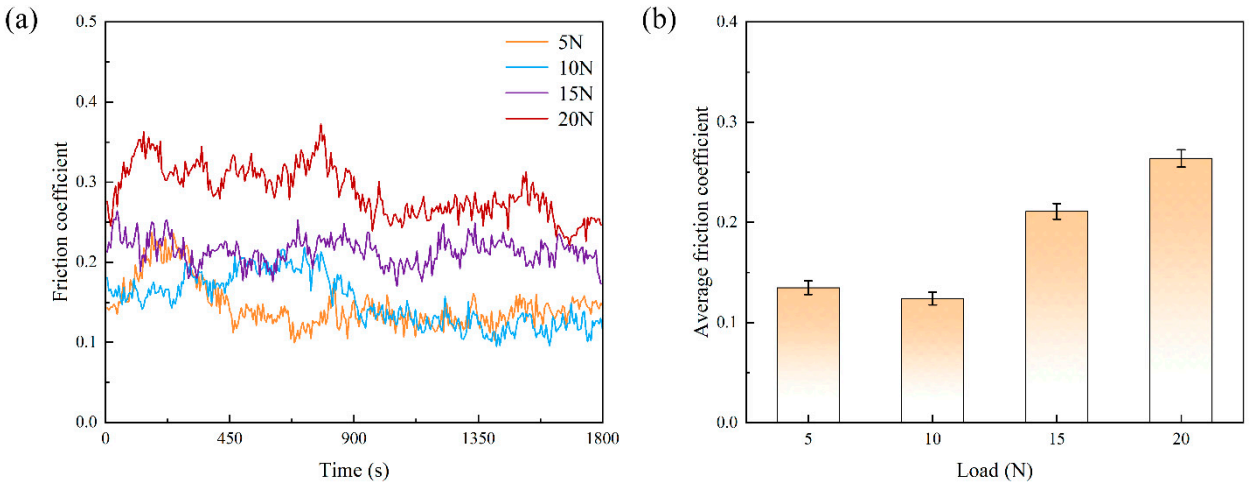

Figure 7. Friction coefficient of different loads. (**a**) Curves over 30 min. (**b**) Average friction coefficients in the last 15 min.

4.4. Effect of BSA Concentration on the Friction Properties of ZrO_2–PEEK Artificial Knee Joints

The concentration of an appropriate lubricant is of great consequence with regard to the enhancement of friction performance. To determine the optimum BSA concentration to reduce the coefficient of friction, TS2 and a load of 10 N were selected for the experiment, and lubricant concentrations of 15 mg/mL, 30 mg/mL, 45 mg/mL, and 60 mg/mL were chosen to ensure that the BSA could be completely dissolved in 1× PBS. The experimental outcomes are presented in Figure 8. The friction coefficient is observed to decrease with increasing concentration. The overall friction coefficient curve demonstrates a clear tendency to decrease with increasing concentration. Similarly, the average friction coefficient observed in the final 15 min of the experiment also exhibits a decrease with increasing concentration.

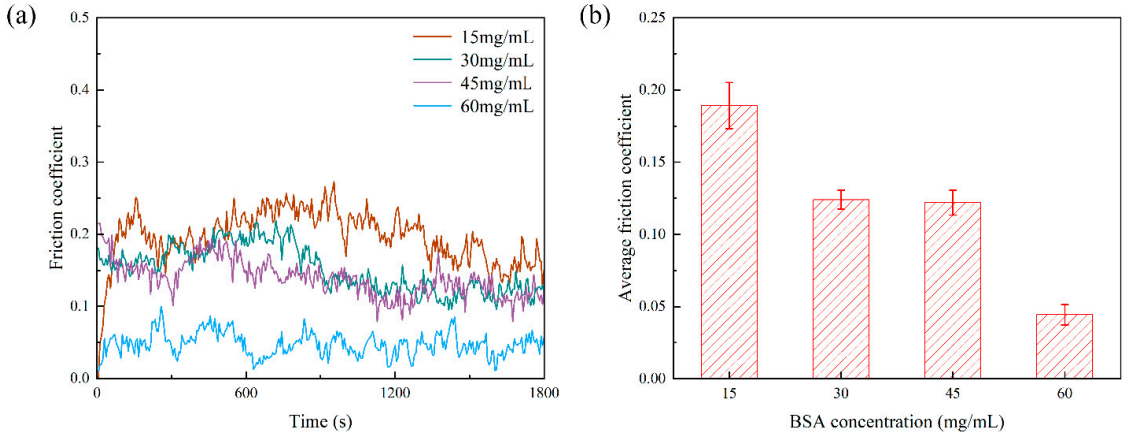

Figure 8. Friction coefficient of different BSA concentrations. (**a**) Curves over 30 min. (**b**) Average friction coefficients in the last 15 min.

4.5. Fluid Flow Simulation Results and Analysis

Figure 9a shows the variation in the lift coefficients of the ball as it passes through different regions at different time steps during the CFD simulation. The ball crosses the textured region at time steps 1150–1250 and 1450–1550, while the rest of the time steps are in the untextured region. The lift coefficient increases significantly when the ball crosses the textured region, which reduces the positive pressure on the ball and decreases the friction coefficient. Figure 9b shows the relative percentage of lift coefficient values for the passage of the ball through the textured and untextured regions (with the lift coefficient defined as 100% for the textured region), as well as the relative percentage of the average friction coefficient between TS0 and TS1 after 15 min (with the friction coefficient defined as 100% for untextured TS0). The discrepancy between the two ratios is less than 5%, which suggests that the simulation results are informative. Figure 10 shows the static pressure distribution of the BSA solution for different time steps, where the view in Figure 10d is perpendicular to the view in the remaining three panels for the untextured region. The pressure distribution shown in Figure 10 indicates that as the PEEK ball passes through the textured region, the highest-pressure region exists with the texture and the fluid pressure in front of the PEEK ball decreases compared to the untextured region. This process reduces the drag force in front of the PEEK ball in the direction of motion, thereby reducing the coefficient of friction. It is worth noting that while the texture at the leading edge of the PEEK ball in the direction of motion primarily provides some space for the flow of the high pressure fluid, the fluid in the texture at the trailing edge of the direction of motion is conducted due to the presence of the negative pressure region, as shown in Figure 13c, and the combined effect of these two further reduces the pressure exerted on the ball.

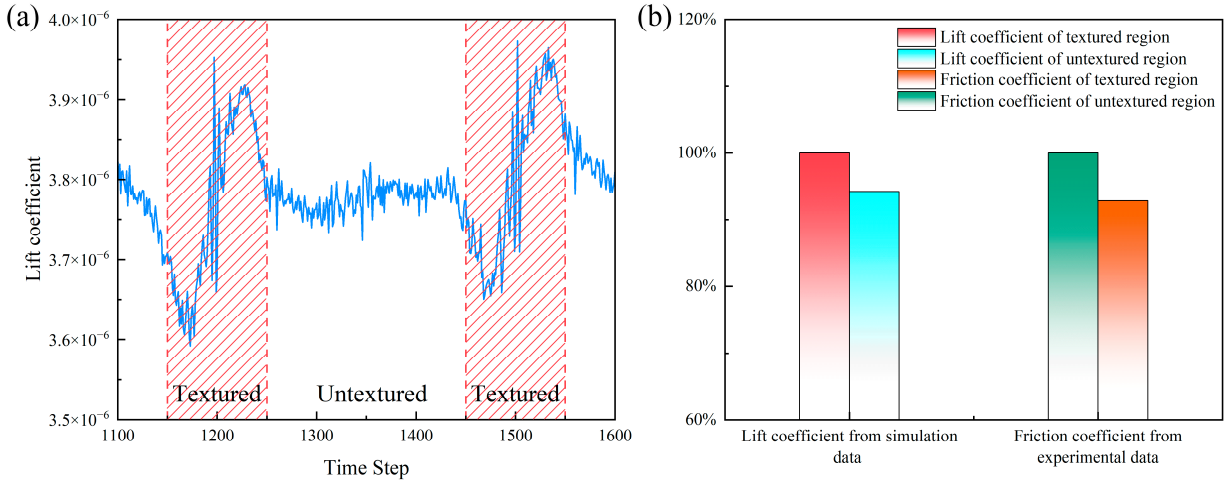

Figure 9. (**a**) Lift coefficient variation curves for different time steps. (**b**) Relative percentage comparison of lift coefficient of simulation data and friction coefficient of experimental data for textured and untextured regions.

Figure 11 shows the velocity magnitude distribution of the BSA solution at different time steps, and Figure 12 shows the velocity vector plots based on the velocity magnitude colouring of the textured region cross-section at different time steps; Figures 11d and 12d apply the same view as Figures 10d and 11a, which show the velocity distribution when the PEEK ball is about to enter the textured region, at which time the BSA solution behind the ball is flowing faster. Additionally, the velocity vector distribution in Figure 12a shows that the BSA solution has a pushing effect on the ball at this time, further reducing the coefficient of friction of the ball as it passes through the textured region. When the time step is 1200, the PEEK ball is in the middle of the textured region. Figure 10b,d show that the velocity and pressure distributions at this time are very close to those in the untextured

region, and the trajectories in Figure 13b (coloured based on the magnitude of the velocities) show that turbulence is generated in the textured region at this time, resulting in the fact that even though the velocity and pressure distributions are close to those in the untextured region, the lift coefficient becomes suddenly large at this point. When the PEEK ball is about to leave the texture region—its path line is shown in Figure 13c—at this time, the liquid in the texture is slightly brought out of the texture due to the existence of a negative pressure region at the back of the ball's movement direction, the turbulence phenomenon is alleviated, and the movement of the liquid obstructs the movement of the PEEK ball so that the drag force of the ball is gradually increased until it completely leaves the texture region. In this process, the lift coefficient gradually stabilises over time and then enters the next texture region.

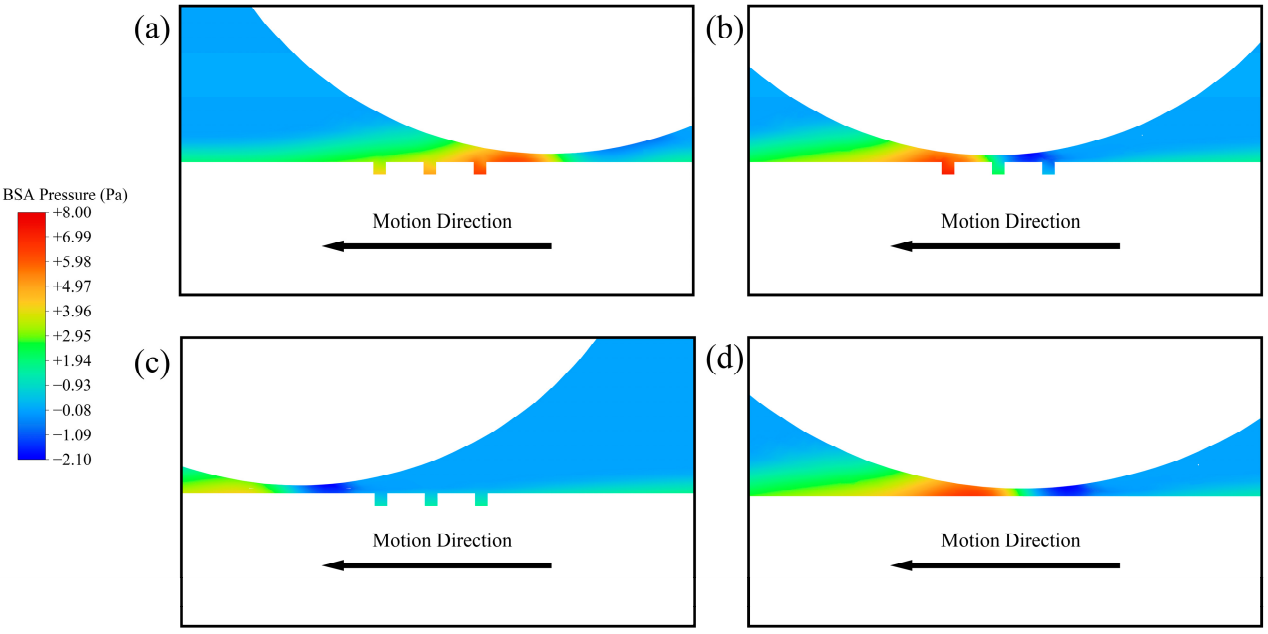

Figure 10. Static pressure distribution of BSA solution at different time steps. (**a**) Time Step 1150. (**b**) Time Step 1200. (**c**) Time Step 1250. (**d**) Time Step 1350.

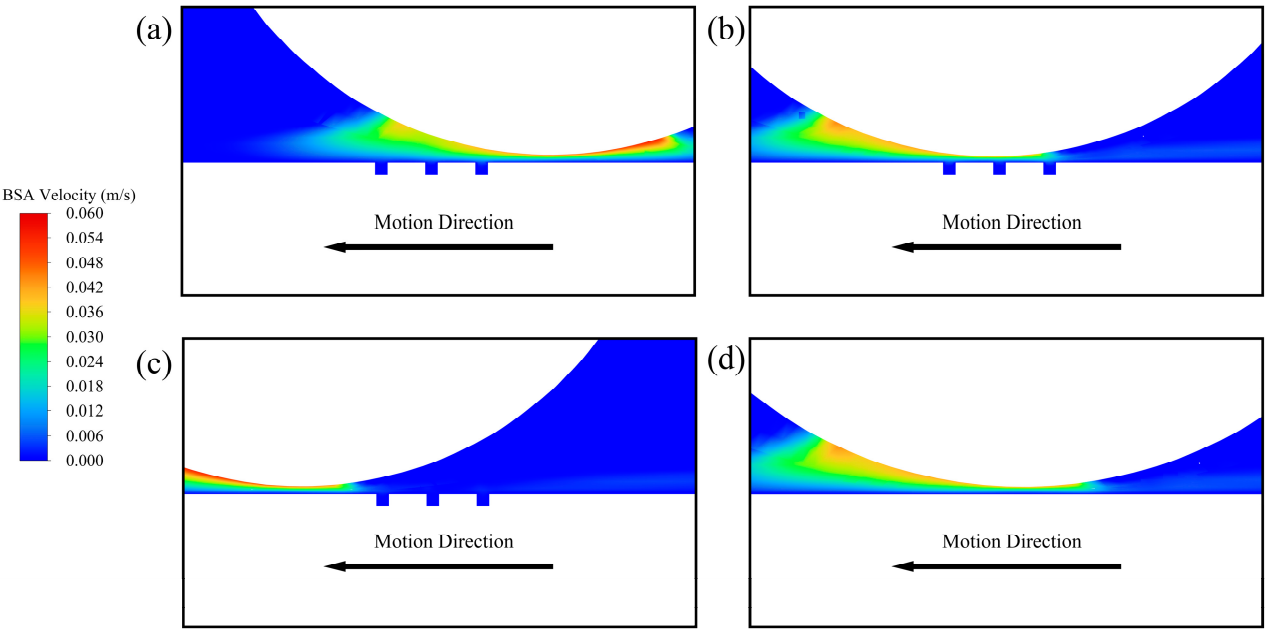

Figure 11. Velocity magnitude distribution of BSA solution at different time steps. (**a**) Time Step 1150. (**b**) Time Step 1200. (**c**) Time Step 1250. (**d**) Time Step 1350.

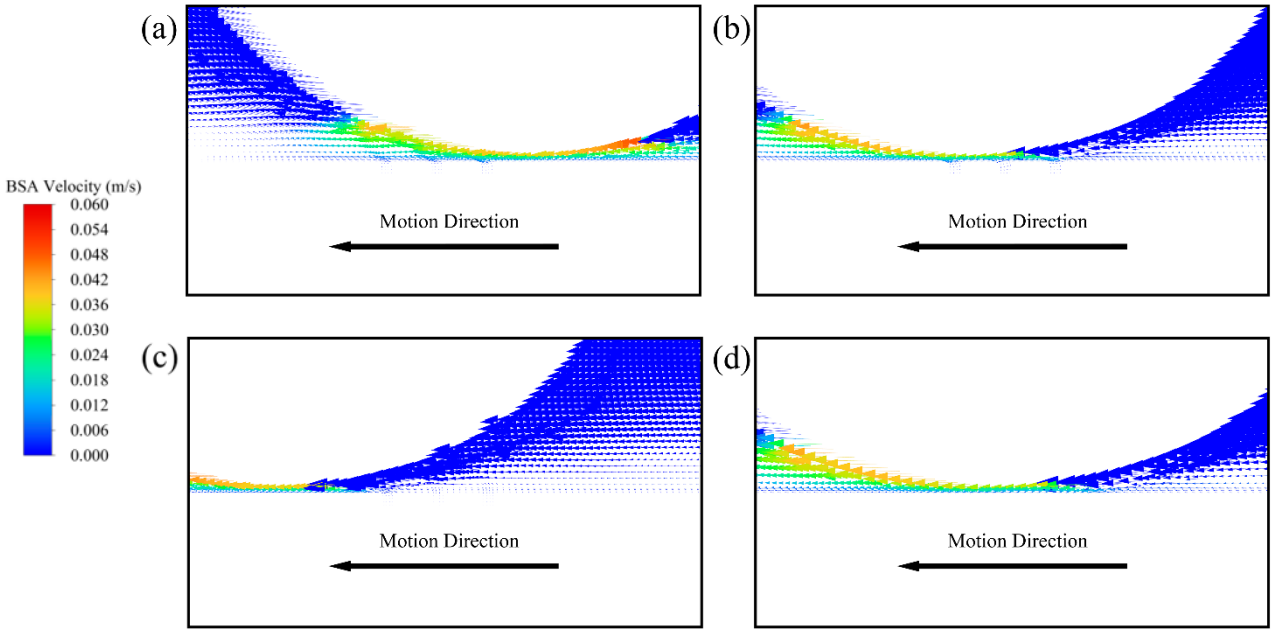

Figure 12. Velocity vector maps of texture region cross-sections coloured based on velocity magnitude at different time steps. (**a**) Time Step 1150. (**b**) Time Step 1200. (**c**) Time Step 1250. (**d**) Time Step 1350.

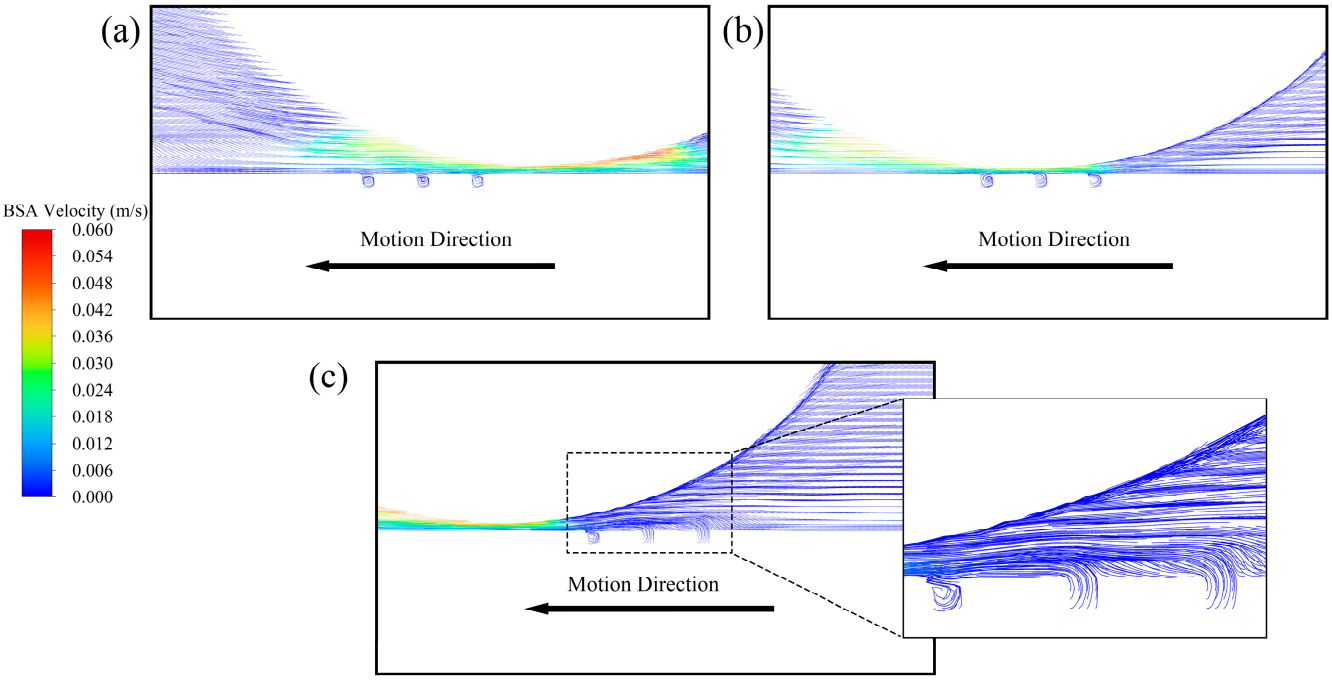

Figure 13. Path lines of BSA solution at different time steps. (**a**) Time Step 1150. (**b**) Time Step 1200. (**c**) Time Step 1250.

4.6. Analysis of ZrO_2–PEEK Artificial Knee Joint Surface Residues

Figure 14 shows the wear phenomenon on the surface of different textured structures after friction wear experiments, which were taken using the super-depth field microscope; this wear phenomenon is hardly visible under the scanning electron microscope, which is consistent with the wear resistance of ZrO_2. TS2 has the lowest visibility of wear marks, indicating the lowest level of wear, which corresponds to its lowest friction coefficient.

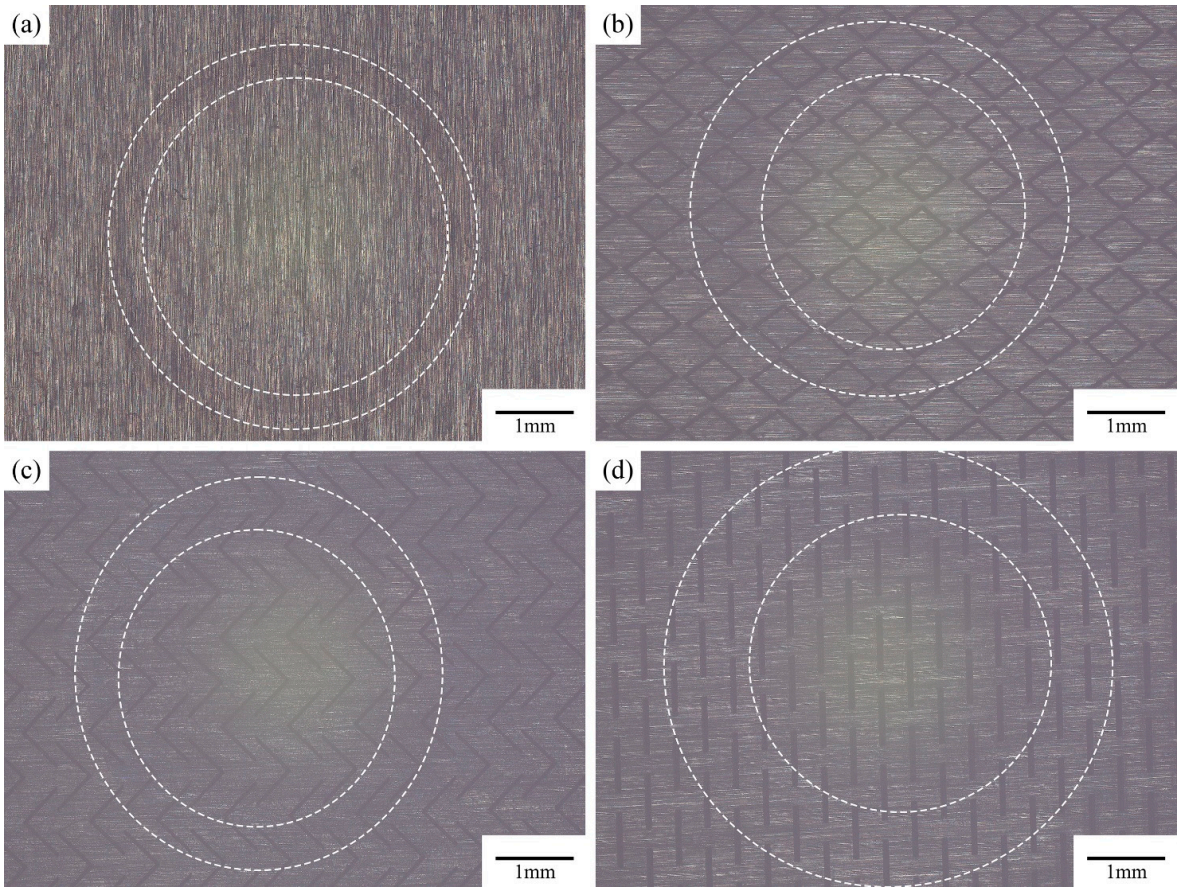

Figure 14. Surface wear of ZrO_2 with different texture structures after friction wear experiments. (**a**) TS0, (**b**) TS1, (**c**) TS2, and (**d**) TS3.

As shown in Figure 15, SEM images, along with magnified views of the corresponding areas, for various surface textures are presented under experimental conditions—a BSA concentration of 30 mg/mL and an applied load of 10 N. The direction of motion is from right to left. The images demonstrate that across different textures and under the same motion direction, the PEEK plastic residues exhibit consistent behaviour, predominantly accumulating near the leading edge of the textures. In contrast, for TS3, significantly less residue is observed, with a distinct textured area consistently appearing along the ball's movement path. Fluid flow simulation results indicate a marked reduction in the normal force exerted on the ball as it passes over the textured region. This explains why, despite TS3 exhibiting lower hydrophilicity compared to TS2, its friction coefficient after 15 min remains comparable to that of TS2.

For the EDS mapping images of different textures under the corresponding magnified regions in Figure 15, the results show that the residues in these textures are higher in C and lower in Zr, and the opposite is true outside the textures, indicating that the residues in the textures are mainly plastic stripped from the PEEK ball. The line scan results for the TS3 texture are shown in Figure 16, where the direction of motion of the PEEK ball is from left to right. In the line scan, the elemental distribution of carbon in the region of the leading edge of the texture is significantly higher than that in the region of the trailing edge of the texture, while the elemental distribution of zirconium is the opposite; these results further confirm that the PEEK plastic is mainly attached to the leading edge of motion direction of the texture.

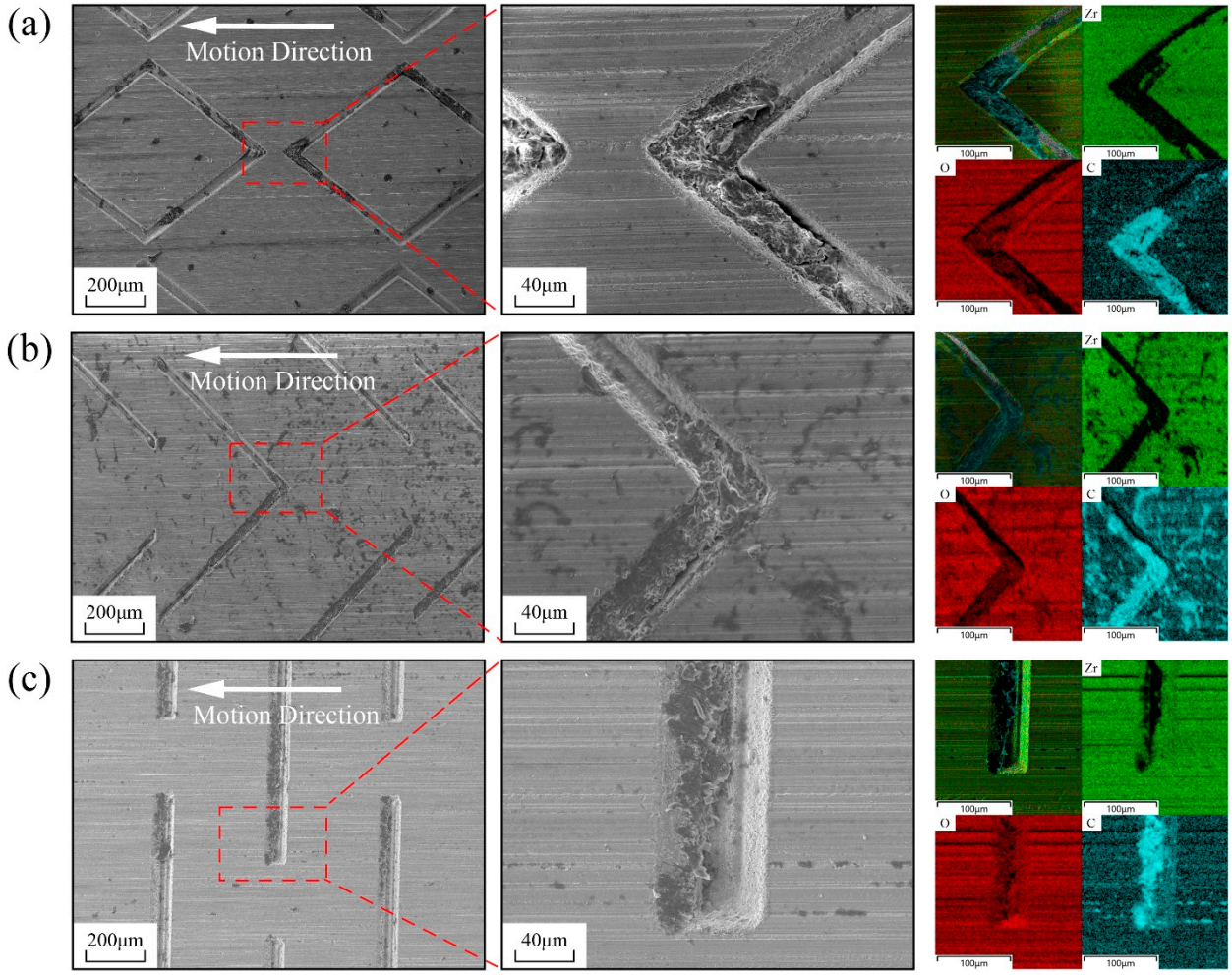

Figure 15. Residual patterns of various textures in the same motion direction. (**a**) TS1, (**b**) TS2, and (**c**) TS3.

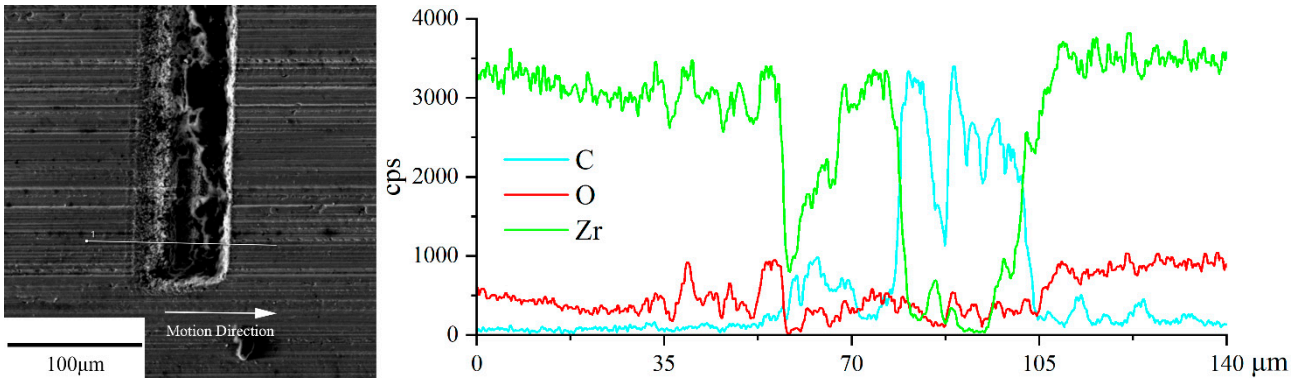

Figure 16. Elemental distribution results from EDS line scan.

The textured regions provide an adequate space for the storage of the PEEK residue and the lubricating fluid, which allows the ball to be immersed in the lubricating fluid for a longer period of time. Furthermore, these textured regions provide sufficient space for the flow of the lubricating fluid when the ball is in motion, which effectively reduces the fluid pressure at the front of the ball's direction of movement and reduces the resistance. Subsequently, as the ball traverses the textured regions, the lubricant within these textured structures is expelled due to the negative pressure, and the push force on the ball further reduces the resistance to movement. The appropriate quantity of PEEK residue can effec-

tively regulate the width and depth of the texture structure, providing a flatter space for the ball to move when it is smoothed at the bottom. The capacity for storing PEEK residue differs between texture structures. The results presented in Figure 15 demonstrate that TS2 exhibits a stronger storage capacity and a more uniform distribution of PEEK residue, whereas the distribution of PEEK residue in TS1 and TS3 is more random. Consequently, the friction coefficients and their fluctuations in the latter 15 min of TS1 and TS3 are larger than those of TS2.

5. Conclusions

The friction and wear properties of ZrO_2–PEEK artificial knee joints with symmetrically textured surfaces were investigated, and fluid flow simulations were carried out to study the effect of the texture structure on the flow characteristics of the lubricant. The following conclusions were drawn from this study:

(1) The experiments and simulations show that a textured surface reduces the coefficient of friction in wet conditions and improves the friction performance of ZrO_2–PEEK knee joints. TS2 showed the greatest improvement, with a 53% reduction in friction over the last 15 min compared to TS0. The best performance was observed at a 10 N load, and the lowest average friction was found at a lubricant concentration of 60 mg/mL.

(2) Fluid flow simulation shows an increase in lift coefficient as the PEEK passes through the textured area. The pressure distribution plots show that before and during the passage of the PEEK ball through the textured region, the textured region reduces the fluid pressure in front of the ball. However, after the ball has passed through the textured region, the fluid pressure in front of the ball increases, resulting in an increase in drag.

(3) The PEEK ball leaves plastic residue on the leading edge of motion direction of the texture and flattens the bottom surface due to abrasion. In TS1, some areas are filled with PEEK residue, causing the ball to move on a nearly flat surface in the last 15 min, resulting in a friction coefficient similar to that of the untextured TS0. In contrast, TS2 and TS3 retain areas not filled with PEEK residue, allowing lubricant to flow in. Fluid flow simulations show that these zones maintain a low lubricant pressure in front of the PEEK balls, reducing the drag of their movement.

The textured ZrO_2–PEEK artificial knee joint proposed in this paper effectively reduces the friction coefficient and significantly improves the service life during motion, which strongly supports the wide application of high-performance artificial knee joints. In addition, this paper also investigates the fluid flow state of the ball as it passes through the textured region, which partially reveals the intrinsic mechanism of the textured structure to reduce friction. In subsequent studies, the coupling of fluid flow simulation and conventional friction and wear simulation can be further explored to study the interaction between the lubricant and the PEEK residue in more detail and to further reveal the wear reduction mechanism of the textured structure.

Author Contributions: Methodology, Y.L.; Software, N.J.; Validation, B.L. and N.J.; Formal analysis, L.J., F.J. and Y.L.; Investigation, L.J., F.J. and K.Z.; Data curation, L.J. and G.W.; Writing—original draft, L.J.; Writing—review & editing, Y.L.; Visualization, G.W.; Supervision, K.Z.; Project administration, Y.L. and C.W.; Funding acquisition, K.Z. and C.W. All authors have read and agreed to the published version of the manuscript.

Funding: This research was funded by the National Natural Science Foundation of China (No. 52305495, No. 52475390, No. 52375197) and the China Postdoctoral Science Foundation (No. 2024M762283).

Data Availability Statement: The raw data supporting the conclusions of this article will be made available by the authors on request.

Conflicts of Interest: The authors declare no conflict of interest.

References

1. Schwartz, A.M.; Farley, K.X.; Guild, G.N.; Bradbury, T.L., Jr. Projections and Epidemiology of Revision Hip and Knee Arthroplasty in the United States to 2030. *J. Arthroplast.* **2020**, *35*, S79–S85. [CrossRef]
2. Klug, A.; Gramlich, Y.; Rudert, M.; Drees, P.; Hoffmann, R.; Weißenberger, M.; Kutzner, K.P. The projected volume of primary and revision total knee arthroplasty will place an immense burden on future health care systems over the next 30 years. *Knee Surg. Sports Traumatol. Arthrosc. Off. J. ESSKA* **2020**, *29*, 3287–3298. [CrossRef] [PubMed]
3. Liu, Y.; Zhu, Q.; Wang, C.; Li, J. Tribological behavior of CoCrMo artificial knee joint with symmetrically biomimetic textured surfaces on PEEK. *Opt. Laser Technol.* **2023**, *157*, 108774. [CrossRef]
4. Feng, C.; Cao, Y.; Wu, T.; Cen, J.; Chen, K.; Li, X.; Zhang, D. Friction and wear mechanism of artificial joint composite material PEEK/ZnO under different decomposition motion modes of knee joint. *Tribol. Int.* **2023**, *189*, 108917. [CrossRef]
5. Bahçe, E.; Emir, E. Investigation of wear of ultra high molecular weight polyethylene in a soft tissue behaviour knee joint prosthesis wear test simulator. *J. Mater. Res. Technol.* **2019**, *8*, 4642–4650. [CrossRef]
6. Kaur, M.; Singh, K. Review on titanium and titanium based alloys as biomaterials for orthopaedic applications. *Mater. Sci. Eng. C* **2019**, *102*, 844–862. [CrossRef]
7. Skjöldebrand, C.; Tipper, J.L.; Hatto, P.; Bryant, M.; Hall, R.M.; Persson, C. Current status and future potential of wear-resistant coatings and articulating surfaces for hip and knee implants. *Mater. Today Bio* **2022**, *151*, 00270–100270. [CrossRef] [PubMed]
8. Kumar, D.; Rajmohan, T.; Venkatachalapathi, S. Wear Behavior of PEEK Matrix Composites: A Review. *Mater. Today Proc.* **2018**, *5*, 14583–14589. [CrossRef]
9. Luo, C.; Liu, Y.; Peng, B.; Chen, M.; Liu, Z.; Li, Z.; Kuang, H.; Gong, B.; Li, Z.; Sun, H. PEEK for Oral Applications: Recent Advances in Mechanical and Adhesive Properties. *Polymers* **2023**, *15*, 386. [CrossRef]
10. Arevalo, E.S.; Pruitt, A.L. Nanomechanical analysis of medical grade PEEK and carbon fiber-reinforced PEEK composites. *J. Mech. Behav. Biomed. Mater.* **2020**, *111*, 104008. [CrossRef] [PubMed]
11. Bannunah, A.M. Biomedical Applications of Zirconia-Based Nanomaterials: Challenges and Future Perspectives. *Molecules* **2023**, *28*, 5428. [CrossRef]
12. Sharanraj, V.; Ramesha, C.M.; Kavya, K.; Kumar, V.; Sadashiva, M.; Chandan, B.R.; Kumar, M.N. Zirconia: As a biocompatible biomaterial used in dental implants. *Adv. Appl. Ceram.* **2021**, *120*, 63–68. [CrossRef]
13. Jitwirachot, K.; Rungsiyakull, P.; Holloway, J.A.; Jia-Mahasap, W. Wear Behavior of Different Generations of Zirconia: Present Literature. *Int. J. Dent.* **2022**, *2022*, 9341616. [CrossRef]
14. Arena, A.; Prete, F.; Rambaldi, E.; Bignozzi, M.C.; Monaco, C.; Di Fiore, A.; Chevalier, J. Nanostructured Zirconia-Based Ceramics and Composites in Dentistry: A State-of-the-Art Review. *Nanomaterials* **2019**, *9*, 1393. [CrossRef] [PubMed]
15. Prashant, S.; Sheila, B.; Hamidreza, A. On the behaviour of zirconia-based dental materials: A review. *J. Mech. Behav. Biomed. Mater.* **2021**, *124*, 104861.
16. Shen, G.; Zhang, J.; Kang, C.; Fang, F. Study on surface texture patterns for improving tribological performance of bioimplants. *Surf. Coat. Technol.* **2021**, *422*, 127567. [CrossRef]
17. Xu, Y.; Liu, W.; Zhang, G.; Li, Z.; Hu, H.; Wang, C.; Zeng, X.; Zhao, S.; Zhang, Y.; Ren, T. Friction stability and cellular behaviors on laser textured Ti–6Al–4V alloy implants with bioinspired micro-overlapping structures. *J. Mech. Behav. Biomed. Mater.* **2020**, *109*, 103823. [CrossRef] [PubMed]
18. Zhao, C.; Jia, X.; Zhao, Q.; Ma, H.; Yu, Z.; Zhang, Z.; Du, W.; Zhang, H. Research progress on the effect of surface texture on the friction properties of CoCrMo alloys. *Compos. Interfaces* **2024**, *31*, 1269–1290. [CrossRef]
19. Allen, Q.; Raeymaekers, B. The effect of texture floor profile on the lubricant film thickness in a textured hard-on-soft bearing with relevance to prosthetic hip implants. *J. Tribol.* **2020**, *143*, 021801. [CrossRef] [PubMed]
20. Harvey, A.G.; Hill, E.W.; Bayat, A. Designing implant surface topography for improved biocompatibility. *Expert Rev. Med. Devices* **2013**, *10*, 257–267. [CrossRef]
21. Xu, L.C.; Siedlecki, C.A. Surface texturing and combinatorial approaches to improve biocompatibility of implanted biomaterials. *Front. Phys.* **2022**, *10*, 994438. [CrossRef]
22. Naddeo, P.; Laino, L.; La Noce, M.; Piattelli, A.; De Rosa, A.; Iezzi, G.; Laino, G.; Paino, F.; Papaccio, G.; Tirino, V. Surface biocompatibility of differently textured titanium implants with mesenchymal stem cells. *Dent. Mater.* **2015**, *31*, 235–243. [CrossRef] [PubMed]

23. Arslan, A.; Masjuki, H.H.; Kalam, M.A.; Varman, M.; Mufti, R.A.; Mosarof, M.H.; Khuong, L.S.; Quazi, M.M. Surface Texture Manufacturing Techniques and Tribological Effect of Surface Texturing on Cutting Tool Performance: A Review. *Crit. Rev. Solid State Mater. Sci.* **2016**, *41*, 447–481. [CrossRef]
24. Liu, Y.; Deng, J.; Wu, F.; Duan, R.; Zhang, X.; Hou, Y. Wear resistance of carbide tools with textured flank-face in dry cutting of green alumina ceramics. *Wear* **2017**, *372–373*, 91–103. [CrossRef]
25. Xing, Y.; Luo, C.; Wan, Y.; Huang, P.; Wu, Z.; Zhang, K. Formation of bionic surface textures composed by micro-channels using nanosecond laser on Si3N4-based ceramics. *Ceram. Int.* **2021**, *47*, 12768–12779. [CrossRef]
26. Zheng, K.; Yang, F.; Zhang, N.; Liu, Q.; Jiang, F. Study on the Cutting Performance of Micro Textured Tools on Cutting Ti-6Al-4V Titanium Alloy. *Micromachines* **2020**, *11*, 137. [CrossRef]
27. Pratap, T.; Patra, K. Tribological performances of symmetrically micro-textured Ti-6Al-4V alloy for hip joint. *Int. J. Mech. Sci.* **2020**, *182*, 105736. [CrossRef]
28. Ghosh, S.; Choudhury, D.; Roy, T.; Bin Mamat, A.; Masjuki, H.H.; Pingguan-Murphy, B. Tribological investigation of diamond-like carbon coated micro-dimpled surface under bovine serum and osteoarthritis oriented synovial fluid. *Sci. Technol. Adv. Mater.* **2015**, *16*, 035002. [CrossRef] [PubMed]
29. Afoke, N.Y.; Byers, P.D.; Hutton, W.C. Contact pressures in the human hip joint. *J. Bone Jt. Surg. Br. Vol.* **1987**, *69*, 536. [CrossRef]
30. Versteeg, H.K.; Malalasekera, W. *An Introduction to Computational Fluid Dynamics: The Finite Volume Method*; Pearson Education: London, UK, 2007; pp. 72–76.

Disclaimer/Publisher's Note: The statements, opinions and data contained in all publications are solely those of the individual author(s) and contributor(s) and not of MDPI and/or the editor(s). MDPI and/or the editor(s) disclaim responsibility for any injury to people or property resulting from any ideas, methods, instructions or products referred to in the content.